Bond-Dependent Coefficient k_b for New-Generation GFRP Bars

Brahim Benmokrane, M.ASCE[1]; Shehab Mehany[2]; Carol Shield[3]; Antonio Nanni, F.ASCE[4]; and Vicki Brown, M.ASCE[5]

Abstract: The new American Concrete Institute (ACI) design code for glass fiber–reinforced polymer (GFRP)–reinforced concrete (RC) members specifies a single value of 1.20 for the bond-dependent coefficient (k_b) of all types of GFRP bars. This value was chosen based on test data from this project, as well as a compilation of data available in the literature. This paper reports on an experimental study that assessed the k_b for the new generation of GFRP bars from five different manufacturers with different surface types: deformed/ribbed, helically deformed, helically grooved, double-helical wrap/sand-coated, and sand-coated. Two bar sizes (No. 5 and No. 8)—with 15.9 and 25.4 mm nominal diameters representing the typical range of GFRP-reinforcing bars used in practice as longitudinal reinforcement in concrete members subjected to bending—were selected from each of the manufacturers. Five RC beam replicates were used to increase experimental accuracy. Therefore, a total of 60 beams, including 50 beams reinforced with GFRP bars and 10 control beams reinforced with conventional steel bars for comparison purposes, were constructed and tested to failure according to a predetermined test method. Based on the analysis, the study confirms using the bond-dependent coefficient value of 1.20 as adopted in the new ACI design code for GFRP–RC members. This value is recommended for GFRP bars complying with (or exceeding) the material specification listed in the ASTM International standard specification for solid round GFRP bars for concrete reinforcement. **DOI: 10.1061/JCCOF2.CCENG-4341**.

Author keywords: Glass fiber–reinforced polymer; Glass fiber–reinforced polymer (GFRP) bars; Beam; Bond-dependent coefficient; Crack width; Building code; Reinforced concrete.

Introduction

Crack width is an important factor in the design of flexural concrete elements reinforced with glass fiber–reinforced polymer (GFRP) bars because of the relatively low modulus of elasticity of the GFRP bars compared with steel. Notwithstanding the corrosion resistance of GFRP bars, the crack width of GFRP-reinforced concrete (RC) elements must be controlled to ensure other serviceability aspects such as appearance and water tightness. As a result, the design of GFRP–RC flexural elements is often governed by the maximum crack width under service loads. Design guides for GFRP–RC have introduced the bond-dependent coefficient (k_b) to account for the degree of bond between the GFRP bars and the surrounding concrete. Theoretically, k_b is dependent on the manufacturing process, mechanical properties, and surface treatment of the bars; however, test results have shown that k_b is also dependent on concrete strength, bar spacing and size, and crack width (Shield et al. 2019). The crack control provisions in ACI 440.11-22 (ACI 2022) are based on a model developed by Frosch (1999). This model is also used in ACI 318-19 (ACI 2019) for steel RC. In the GFRP–RC formulation, however, a bond-dependent coefficient—k_b—is added to account for differences in bond between GFRP and concrete compared with steel and concrete. Frosch's approach is based on a physical model of cracking, in which the flexural crack width is assumed to vary linearly from zero at the location of the section neutral axis to a maximum at the tension face. Crack width at the level of the reinforcement is presumed to be the crack spacing times the strain in the reinforcement, based on the assumption that the reinforcement is uniformly strained between cracks and that tension stiffening is ignored.

ACI 440.1R-15 (ACI 2015) suggests that the k_b value be determined experimentally using the Canadian test method presented in CSA S806-12 (CSA 2012). When experimental data are not available, ACI 440.1R-15 (ACI 2015) suggests using a conservative value of 1.40 for any type of FRP bars. This conservative value (1.40) is based on data from studies on the first generation of GFRP with a low modulus of elasticity. Analysis of a compilation of experimental data constructed in Shield et al. (2019) recommends that k_b be taken as 1.20 for sand-coated bars and continue to be taken as 1.40 for all other surface deformation types of FRP bars because of insufficient experimental evidence for nonsand-coated bars.

With advancements in manufacturing processes, improved properties of GFRP-bar constituent materials, and higher glass-

[1]Professor of Civil Engineering and Tier 1 Canada Research Chair Professor in Advanced Composite Materials for Civil Structures and Industrial Chair Professor in FRP Reinforcement for Concrete Structures, Dept. of Civil and Building Engineering, Univ. of Sherbrooke, Quebec, QC, Canada J1K 2R1. Email: brahim.benmokrane@usherbrooke.ca

[2]Postdoctoral Fellow, Dept. of Civil and Building Engineering, Univ. of Sherbrooke, Quebec, QC, Canada J1K 2R1. Email: shehab.mehany@usherbrooke.ca

[3]Professor Emeritus, Dept. of Civil, Environmental, and Geo-Engineering, Univ. of Minnesota, Minneapolis, MN 55455. Email: ckshield@umn.edu

[4]Professor, Dept. of Civil and Architectural Engineering, Univ. of Miami, Coral Gables, FL 33146. Email: nanni@miami.edu

[5]Professor, Civil Engineering Dept., Widener Univ., Chester, PA 19013 (corresponding author). ORCID: https://orcid.org/0000-0002-8738-8559. Email: vlbrown@widener.edu

Note. This manuscript was submitted on April 2, 2023; approved on August 23, 2023; published online on October 3, 2023. Discussion period open until March 3, 2024; separate discussions must be submitted for individual papers. This paper is part of the ***Journal of Composites for Construction***, © ASCE, ISSN 1090-0268.

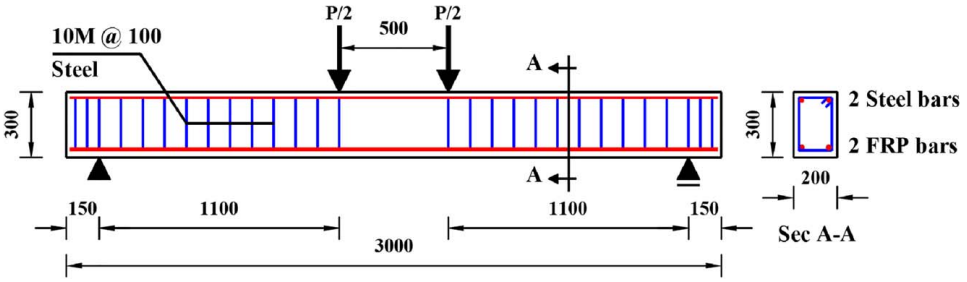

Fig. 1. Reinforcement plan and configuration of beams with the CSA S806 test method (CSA S806-12).

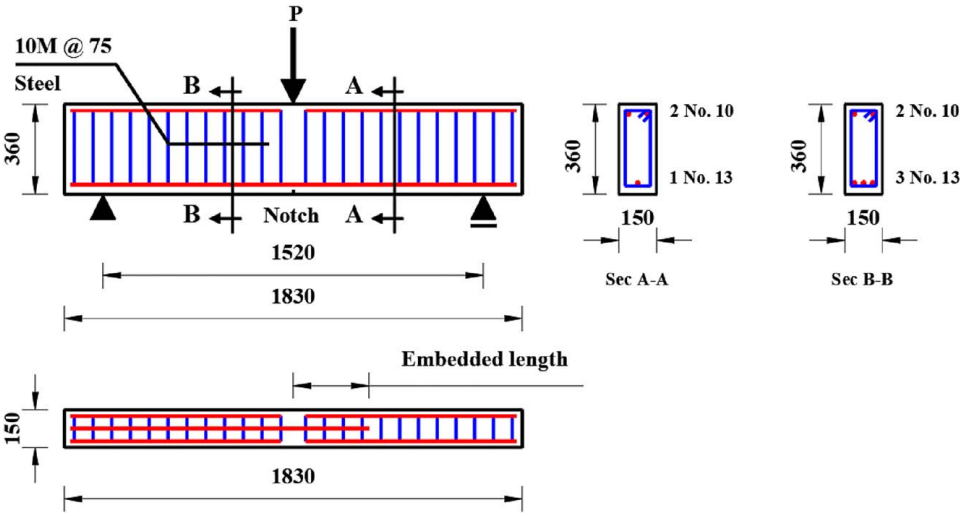

Fig. 2. Reinforcement plan and configuration of beams with the adapted test method (Benzecry et al. 2021).

fiber mass fraction, the latest generation of GFRP bars have better physical and mechanical properties than do the earlier bars (e.g., GFRP bars with a modulus of elasticity greater than 60,000 MPa are commercially available). Therefore, this paper presents new data obtained from laboratory experimentation conducted on the new-generation GFRP-reinforcing bars in RC beams according to the test method proposed by Benzecry et al. (2021). The main objectives of this testing program were (1) to determine k_b via a reliable and repeatable test method that can be standardized; and (2) to determine k_b for the new generation of GFRP bars from five different manufacturers with different surface types.

Test Method Used to Assess k_b

CSA S806-12 (CSA 2012) provides a recommended test for experimentally determining k_b, correlating measured crack width to k_b. This test method has been reported or used by several authors (Newhook 2000; El-Salakawy and Benmokrane 2004; El-Nemr et al. 2016; Elgabbas et al. 2017; Mehany et al. 2021a, b). This test procedure approved by CSA S806-12 (CSA 2012) is based on beam testing under four-point bending. CSA S806-12 (CSA 2012) specifies Eq. (1) based on the research work by Frosch (1999) to determine k_b from the measured service-level crack widths and stresses in the FRP bars during testing.

$$w_{\text{cr}} = 2\frac{f_f}{E_f}\beta k_b\sqrt{d_c^2 + (s/2)^2} \tag{1}$$

where w_{cr} = crack width on the tension face (mm); d_c = distance from the center of the tension bar to the tension face of the concrete (mm); s = bar spacing; E_f = modulus of elasticity of GFRP reinforcement (MPa); β = amplification factor that accounts for the strain gradient, taken as $\beta = (h-c)/(d-c)$; and f_f = GFRP bar stress (MPa), which is calculated from the applied moment, M, as follows:

$$f_f = n_f \times \frac{My}{I_{\text{cr}}} \tag{2}$$

where I_{cr} = moment of inertia of the cracked transformed section; y = distance from the centroid of the cracked transformed section to the centroid of the reinforcing bar; and the modular ratio, n_f, is defined as follows:

$$n_f = \frac{E_f}{E_c} \tag{3}$$

where E_c = modulus of elasticity of concrete, taken as $E_c = 4{,}700\sqrt{f'_c}$ (MPa).

Recently, Benzecry et al. (2021) proposed a new method adapted from that in CSA S806-12 (CSA 2012). The adapted test method has several advantages over the CSA S806-12 (CSA 2012) test method. It uses a notched concrete beam to induce the crack formation at a selected position (notch) versus initiation at any section in a constant moment region that might make it difficult to identify the first crack location. In addition, a three-point load configuration is adopted to allow for a combination of shear and

Table 1. Mechanical properties of the GFRP and steel reinforcement

Bar type	Surface configuration	Bar size	d_b[b] (mm)	$d_{m\text{-ave}}$[d] (mm)	d_{im}[a] (mm)	A_f[b] (mm²)	A_{im}[c] (mm²)	E_f (GPa)	f_{fu} (MPa)	ε_{fu} (%)
GFRP1	Deformed/ribbed	No. 8	25.4	28.9	27.6	510	598	60.0	1,130	1.90
		No. 5	15.9	19.2	18.2	199	259	63.0	1,265	2.00
GFRP2	Helically deformed	No. 8	25.4	27.7	27.1	510	576	63.0	998	2.00
		No. 5	15.9	16.9	17.4	199	237	64.0	1,422	2.00
GFRP3	Helically grooved	No. 8	25.4	27.3	27.0	510	572	61.0	801	1.30
		No. 5	15.9	16.9	17.0	199	227	60.0	1,004	1.70
GFRP4	Double-helical wrap/sand-coated	No. 8	25.4	28.1	27.3	510	584	62.0	1,068	1.70
		No. 5	15.9	17.9	17.7	199	247	62.0	1,281	2.10
GFRP5	Sand-coated	No. 8	25.4	27.5	26.8	510	564	61.0	1,046	1.70
		No. 5	15.9	17.7	17.3	199	236	62.0	1,504	2.40
Steel	Ribbed	25M	25.2	—	—	500	—	E_s[e] = 200	f_y[e] = 450	ε_y[e] = 0.225
		15M	16.0	—	—	200	—	E_s[e] = 200	f_y[e] = 450	ε_y[e] = 0.225
		10M	9.5	—	—	71	—	E_s[e] = 200	f_y[e] = 450	ε_y[e] = 0.225

Note: Properties calculated based on nominal cross-sectional area. The SI equivalents for No. 5 and No. 8 bars are 15M and 25M, respectively.
[a]d_{im} is calculated based on the A_{im}.
[b]Nominal values.
[c]Immersed cross-sectional area (measured).
[d]$d_{m\text{-ave}}$ is determined by measuring the diameter at three different locations using a digital caliper, as described in Benmokrane et al. (2023).
[e]E_s, f_y, and ε_y are the modulus of elasticity, yield strength, and yield strain of the steel bars, respectively.

moment in the cracking zone, which might be more realistic than the pure bending state found in the four-point load configuration. Furthermore, the three-point bending test may be suitable for most laboratories and more practical for smaller beam specimens. This paper renamed this test method as the ACI 440 Test Method, and used it in this study. Figs. 1 and 2 show the details of the test specimens based on CSA S806-12 (CSA 2012) and ACI 440 Test Method, respectively.

Experimental Program

GFRP and Steel Bars

Because k_b is influenced by the performance of the bond between the concrete and the reinforcement, five different types of the new generation of GFRP reinforcement with different surface conditions—deformed/ribbed (GFRP1), helically deformed (GFRP2), helically grooved (GFRP3), double helical wrap/sand-coated (GFRP4), and sand-coated (GFRP5)—were selected for use in this research. The selected GFRP bars are commercially available and have physical and mechanical properties, greatly exceeding some of the requirements of ASTM D7957/D7957M-22 (ASTM 2022) and CSA S807-19 (CSA 2019). The GFRP bars were all near or slightly over the maximum cross-sectional area allowed by ASTM D7957/D7957M-22 (ASTM 2022) as determined by Benmokrane et al. (2023). No. 5 and No. 8 GFRP bars with nominal diameters of 15.9 and 25.4 mm, respectively, and nominal areas of 199 and 510 mm^2, respectively, as per ASTM D7957/D7957M-22 (ASTM 2022) were used. The physical and mechanical properties of these bars were documented by Benmokrane et al. (2023). In addition to the GFRP bars, 15M and 25M steel-grade 450 bars served as longitudinal reinforcement in the reference beams. Furthermore, one size (10M) of steel stirrups was used to fabricate the transverse reinforcement for all beams. Table 1 summarizes the mechanical properties of the GFRP and steel bars. Fig. 3 is a photograph of the GFRP bars, illustrating the different surface characteristics. More details of the physical and mechanical properties of the GFRP bars can be found in Benmokrane et al. (2023).

Concrete

The beams were constructed in the laboratory at the University of Sherbrooke with ready-mixed normal-weight concrete (NWC) with a specified 28-day compressive strength of 35 MPa. The NWC mixture proportions per cubic meter were 272 and 730 kg of coarse aggregates (crushed stone) in size ranges of 5–10 and 5–20 mm, respectively; 719 kg of fine aggregates (crushed stone); 244 kg of cement (Type GU), 216 kg of cement (Type GUb-SF); 0.35 water-to-cement ratio (w/c); 80 mL/100 kg of entrained air admixture; and 300 mL/100 kg of water-reducing agent. The concrete compressive strength of 41.7 ± 0.3 MPa was obtained at the time of beam testing on three 100×200 mm concrete cylinders in accordance with ASTM C39/C39M-21 (ASTM 2021).

Beam Details and Test Matrix

Five identical RC beam repetitions were used to ensure experimental accuracy and to investigate the repeatability of the test method under identical conditions. Therefore, a total of 60 specimens—including 50 RC beams with GFRP bars and 10 with steel bars as

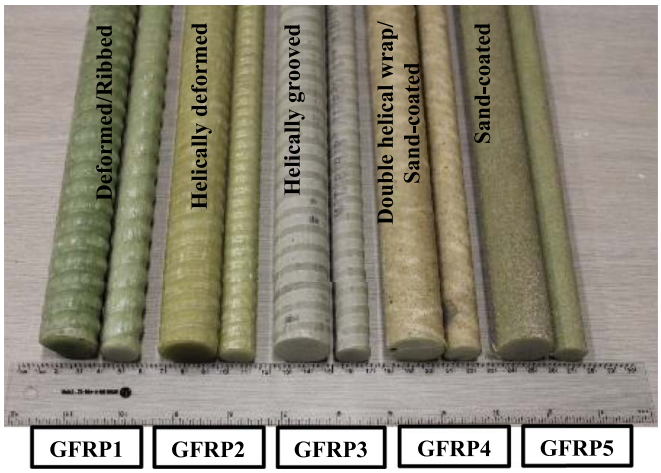

Fig. 3. GFRP bar types and surface characteristics.

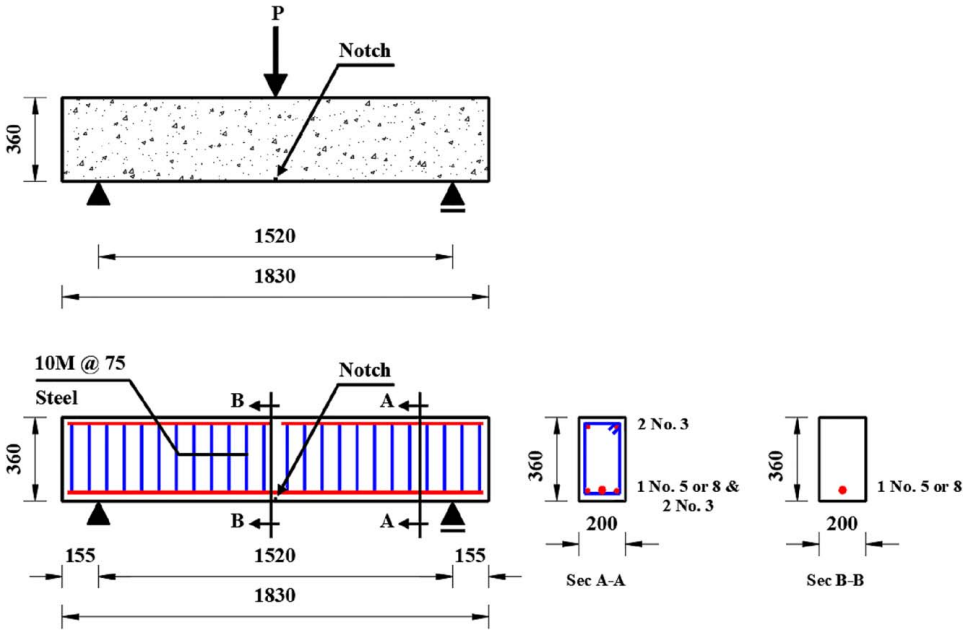

Fig. 4. Dimensions, reinforcement details, and strain-gauge locations of the test specimens (dimensions in mm).

reference—were constructed and tested. Each specimen measured 360 mm in depth, 200 mm in width, and 1,830 mm in total length. The test span was 1,520 mm with overhangs of 155 mm above both supports to ensure appropriate bar anchorage. The clear bottom cover to the stirrups was 38 mm. The bottom bars included three GFRP bars, but only one bar (No. 5 or No. 8) ran continuously through the center of the span as tension reinforcement. All specimens were reinforced with two No. 3 GFRP bars as top reinforcement to hold the stirrups. The top bars were interrupted over the center (100 mm) to prevent them from acting as tension (or compression) reinforcement. Moreover, 10M-steel stirrups spaced at 75 mm were used in the transverse direction to prevent shear failure. Fig. 4 presents the specimen geometry and reinforcement details. Table 2 gives the test matrix and details of the test specimens. Each beam was identified with a label consisting of letters and numbers, beginning with G1, G2, G3, G4, or G5, referring to the type of longitudinal reinforcement: deformed/ribbed, helically deformed, helically grooved, double helical wrap/sand-coated, or sand-coated, respectively. The numbers 15 and 25 correspond to No. 5 and No. 8 bars, respectively (the acronym corresponds to the bar size in mm because the SI System is used throughout the paper), followed by the specimen number.

Table 2. Test matrix and details of test specimens reinforced with No. 5 or No. 8 GFRP or steel bars

Beam ID ("X" = specimen number, i.e., 1, 2, 3, 4, or 5)	Amount of reinforcement in the test section	ρ_f (%)	E_rA_r, $N \times 10^6$
G1-15-X	1 No. 5	0.33	12.5
G2-15-X	1 No. 5	0.33	12.7
G3-15-X	1 No. 5	0.33	11.9
G4-15-X	1 No. 5	0.33	12.3
G5-15-X	1 No. 5	0.33	12.3
S-15-X	1–15M	0.33	40
G1-25-X	1 No.8	0.85	30.6
G2-25-X	1 No. 8	0.85	32.1
G3-25-X	1 No. 8	0.85	31.1
G4-25-X	1 No. 8	0.85	31.6
G5-25-X	1 No. 8	0.85	31.1
S-25-X	1–25M	0.84	100

Note: The SI equivalents for No. 5 and No. 8 bars are 15M and 25M, respectively.

Test-Specimen Fabrication

GFRP and steel reinforcement cages were assembled with tie wraps outside the formwork. The beam specimens were prepared and carefully placed inside the wooden formwork for casting. Plastic spacers were used to keep the reinforcement cage at the correct distance from the mold sides, as shown in Fig. 5. One hour after casting, the beams were covered with wet burlap and plastic sheeting for curing. The concrete cylinders were cast and cured under the same conditions as the beams.

Measurement Equipment, Test Setup, and Procedure

Before testing began, the beams were notched at midspan to induce a localized crack and facilitate crack monitoring. A 15 mm by 15 mm notch size was chosen after the first three beams (G1-15-1, G1-15-2, and G1-15-3) were tested with smaller notches (4, 8, and 12 mm in width, respectively) that resulted in the first crack not forming at the notch as intended. The beam surface was painted white and marked with grid lines (100 × 100 mm) to facilitate the observation of crack propagation. Each specimen

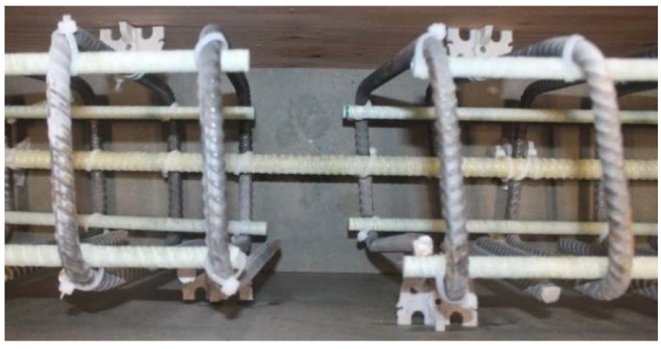

Fig. 5. Typical beam prior to casting.

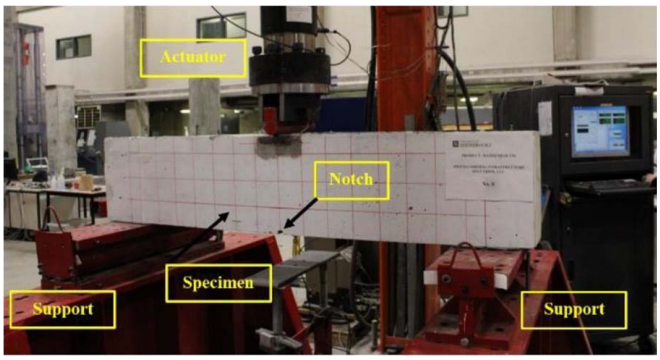

Fig. 6. Test setup.

was simply supported over a free span of 1,520 mm with one end on a roller support and the other on a hinged support attached to two steel plates (width = 150 mm).

Beam instrumentation included two high-accuracy linear variable differential transformers (LVDTs) that were placed horizontally at the level of the reinforcement at the notch location to record crack widths. One LVDT [LVDT (1)] was placed on one of the beam side faces prior to the start of the test because the notch was intended to induce the crack at that location. The beams were tested under three-point bending as proposed by Benzecry et al. (2021). The load was applied with a 1,000 kN hydraulic actuator in two phases. In the first phase, the load was applied in load-controlled mode at a rate of 5 kN/min up to a value corresponding to a midspan moment of approximately 21.6 kN·m. This load was equal to 1.25 times the theoretical cracking moment $M_{cr} = 17.3$ kN·m, calculated using gross-section properties and assuming a modulus of rupture of $0.62\sqrt{f'_c}$ per ACI 440.1R-15 (ACI 2015). The level of loading was approximately 33%–38% of nominal moment capacity for the beams reinforced with No. 5 GFRP bars and approximately 23% for beams reinforced with No. 8 GFRP bars. Unloading stopped at a value corresponding to a midspan moment of 2.6 kN·m ($0.15M_{cr}$ in load control at a rate of 10 kN/min) to keep the equipment engaged. The test was paused for about 3 min to visually measure the crack width at the level of the reinforcement with a handheld microscope and to install the other LVDT [LVDT (2)] on the other side face of the beam. In the second phase, the beam was loaded in displacement-control at a rate of 1.2 mm/min until failure. The shift from load control to displacement control was chosen to avoid a catastrophic collapse and to observe the cracking behavior of the beam. Fig. 6 provides the details of the test setup.

Experimental Results and Discussions

Definition of Service-Load Level

Previous research has shown that k_b is highly dependent on crack width (Shield et al. 2019), with k_b increasing with increased crack width. Because GFRP reinforcement is free from corrosion, the flexural crack width limits specified in FRP–RC design standards are more relaxed than those for steel-RC members. The approach taken to calculate k_b was based on the maximum allowable crack width. The flexural distribution requirements in Chapter 24 of ACI 440.11-22 (ACI 2022) are based on maximum crack widths of 0.71 mm at the extreme tension face of the section, which is considered acceptable for aesthetic and performance reasons. As the LVDTs were placed at the level of the reinforcement, k_b was calculated using the value of load and corresponding moment that occurred when the LVDT crack width measurements were 0.59 mm for the No. 5 GFRP bar specimens and 0.57 mm for the No. 8 GFRP bar specimens (theoretically corresponding to 0.71 mm crack widths at the extreme tension face), based on the assumption that the crack width varies linearly with depth from the elastic cracked-section neutral axis. For the steel-RC beams, k_b was determined for an extrapolated bottom surface crack width of 0.41 mm, which corresponds to the crack width used in the crack control provisions in ACI 318-19 (ACI 2019).

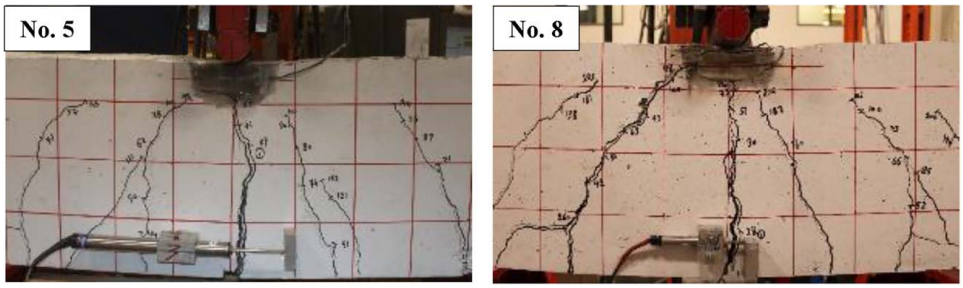

Fig. 7. Typical crack pattern of the RC beams with No. 5 and No. 8 (SI equivalent: 15M and 25M) GFRP1 bars.

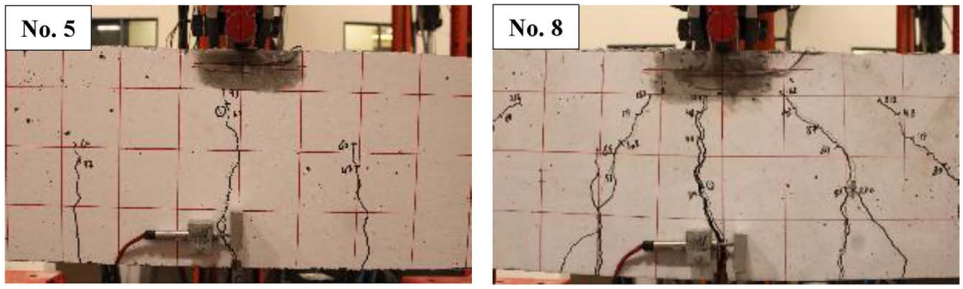

Fig. 8. Typical crack pattern of the RC beams with No. 5 and No. 8 (SI equivalent: 15M and 25M) GFRP2 bars.

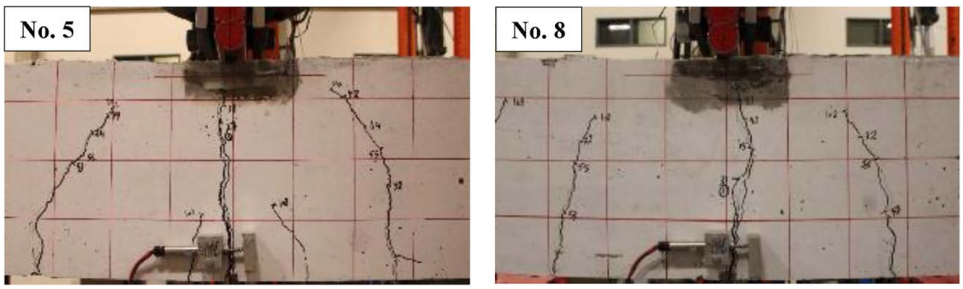

Fig. 9. Typical crack pattern of the RC beams with No. 5 and No. 8 (SI equivalent: 15M and 25M) GFRP3 bars.

Crack Propagation

Figs. 7–12 present the typical crack patterns of the test specimens during testing. The first crack typically occurred at the notch once the concrete's tension capacity had been exceeded. Exceptions were G1-15-1, G1-15-2, and G1-15-3 with smaller notches, as well as G3-15-2, G4-25-4, G4-25-5, and S-25-1, for which the coarse aggregate distribution in the concrete and the hairy cracks from shrinkage before testing may have had some effect on the first crack path. As more load was applied, the crack widened and propagated progressively vertically, while new cracks appeared along the specimen's span until failure. It was observed that, because of the relatively low modulus of elasticity of the GFRP bars, the beams reinforced with GFRP bars developed wider and deeper cracks than the beams reinforced with steel bars. Lastly, all the beam specimens clearly failed in flexure, regardless of the bar type (steel or GFRP), bar size (No. 5 or No. 8), or the surface treatment.

Evaluation of the Bond-Dependent Coefficient (k_b)

Data Processing

Beams with First Crack Not Located at Midspan. Data for beams that had the crack location outside of the region where there was just the single bottom longitudinal bar (Beams G1-15-1, G1-15-2, G1-15-3, G3-15-2, G4-25-4, G4-25-5, and S-25-1 as previously discussed) were discarded from analysis because the crack occurred where the two additional No. 3 longitudinal bars were located. Therefore, the correct value of "s" for use in the k_b equation was not known in this situation because these additional bars were not fully developed.

LVDT Adjustments. For the beams in which both LVDT (1) and LVDT (2) data were available, the values of LVDT (1) and LVDT (2) were adjusted by subtracting the difference between the visually measured crack width [the initial reading in LVDT (2)] and the corresponding value in LVDT (1) from the LVDT (1) values. This adjustment ensured that the visually measured crack width after the unloading phase matched the corresponding value in LVDT (1) accurately. Plots of applied midspan moment versus measured crack width at the height of the LVDTs for each of the beams that had the crack location at the notch where there was just the single bottom longitudinal bar are shown in Figs. 13–24. The dashed lines in these figures represent the readings from LVDT (1) after adjusting the reading to match the LVDT (2) reading at unloading; the solid line represents LVDT (2), which was attached after unloading and just prior to the second phase of loading.

The two LVDTs track almost perfectly during the second phase of loading, indicating that the crack was opening similarly on both

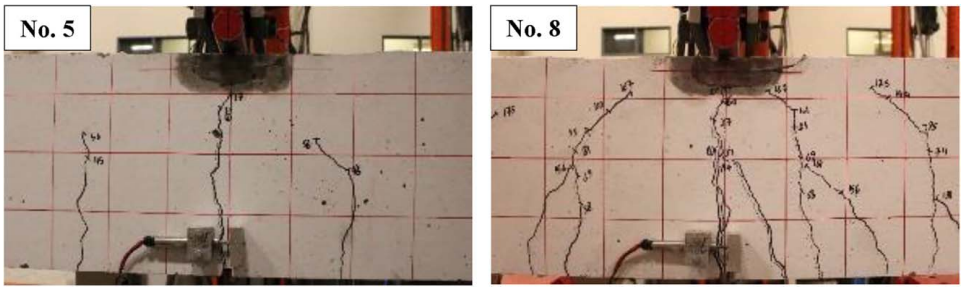

Fig. 10. Typical crack pattern of the RC beams with No. 5 and No. 8 (SI equivalent: 15M and 25M) GFRP4 bars.

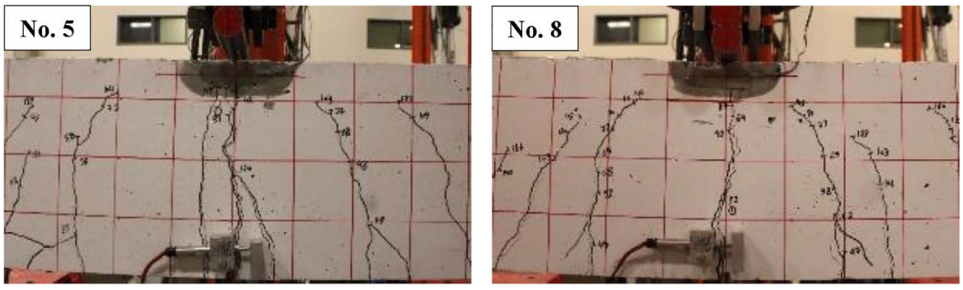

Fig. 11. Typical crack pattern of the RC beams with No. 5 and No. 8 (SI equivalent: 15M and 25M) GFRP5 bars.

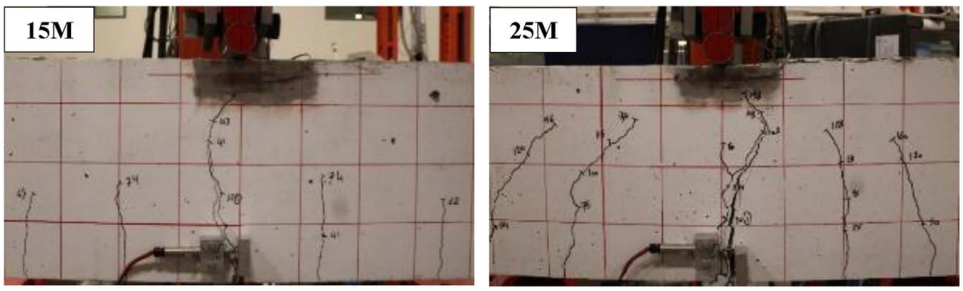

Fig. 12. Typical crack pattern of the RC beams with steel bars.

sides of the beam. It is reasonable to assume that the LVDT (1) measurements are equal to the crack opening during unloading and the part of the first loading after cracking occurred. The theoretical relationship between the crack width at the level of the LVDT and the bottom fiber crack width is $w_{\text{bottom fiber}} = w_{\text{LVDT}}\beta$, where $w_{\text{bottom fiber}}$ is the extrapolated crack width at the bottom of the beam; w_{LVDT} is the crack width measured by the LVDTs; and β is the amplification factor that accounts for the strain gradient, taken as $\beta = (h - c)/(d - c)$. In this investigation, β is equal to 1.242 and 1.205 for the specimens with No. 8 and No. 5 bars, respectively. Therefore, a crack width of 0.71 mm at the tension face would correspond to a crack width of 0.57 mm at the location of the LVDT for beams with No. 8 bars and 0.59 mm at the location of the LVDT for beams with No. 5 bars.

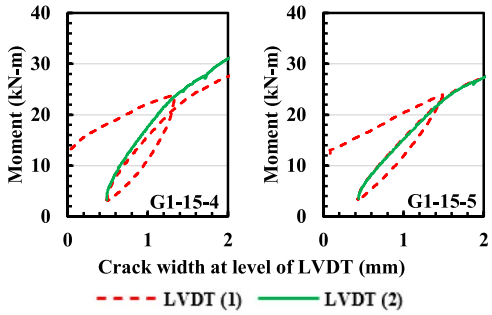

Fig. 13. Moment versus crack width for beams reinforced with No. 5 (SI equivalent: 15M) GFRP1 bars.

Goodness of fit between the two LVDTs over the range from the initiation of the second phase of loading until a bottom fiber crack estimate of 0.71 or 0.41 mm based on LVDT (2) for the GFRP- and steel-RC beams, respectively, were calculated with the estimates of mean absolute percentage error (MAPE). Table 3 provides the values of these error estimates for the beams for which both LVDT (1) and LVDT (2) data were obtained. The MAPE estimate provides an average percentage error between readings. Most of the GFRP beams show good agreement (less than an average error of 5%) between the crack-width measurements recorded by the two LVDTs, with the exception of Beams G5-25-2 and G5-25-4. Some difference between the two LVDT readings is to be expected given that the cracks are likely to grow slightly differently on the two sides of the beam. Given the general good agreement between

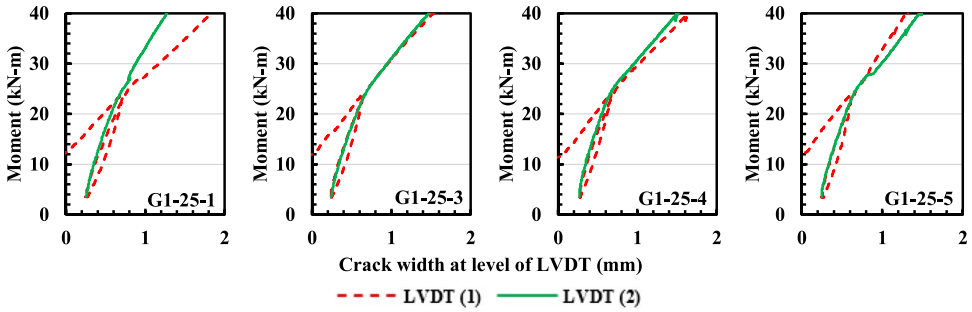

Fig. 14. Moment versus crack width for beams reinforced with No. 8 (SI equivalent: 25M) GFRP1 bars.

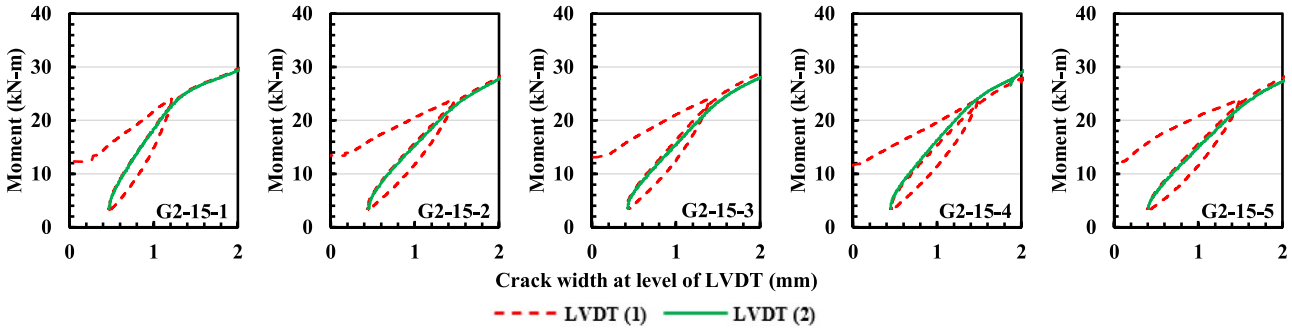

Fig. 15. Moment versus crack width for beams reinforced with No. 5 (SI equivalent: 15M) GFRP2 bars.

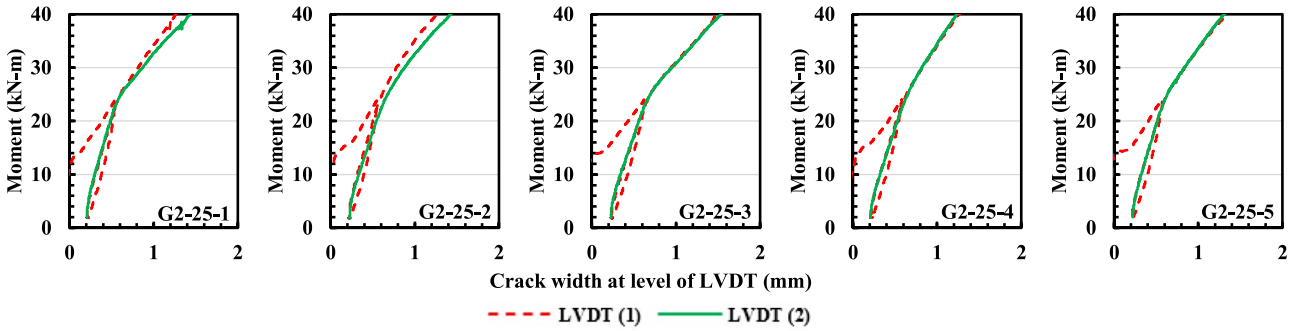

Fig. 16. Moment versus crack width for beams reinforced with No. 8 (SI equivalent: 25M) GFRP2 bars.

the readings, it appears that the readings from either LVDT can be used to determine k_b for GFRP–RC beams.

Crack Widths at the First Peak Load (First Phase of Loading). Each beam was initially loaded to around 62 kN (23.56 kN·m) before unloading and installing LVDT (2). At that point, 47 beams (39 GFRP–RC beams and 8 steel-RC beams) had the first crack at midspan and included data from LVDT (1). Therefore, only these beams were analyzed. The average first peak load was 61.7 kN (23.45 kN·m), with a COV of 1.0% and a range of 58.4 to 62.1 kN (22.20–23.60 kN·m). As expected, the peak load in the initial loading was very consistent for all 47 beams. Fig. 25 shows a plot of crack width at the level of the reinforcement from LVDT (1) at a load corresponding to the first peak load by bar size and type. In Fig. 25, respective crack widths of 0.59 mm

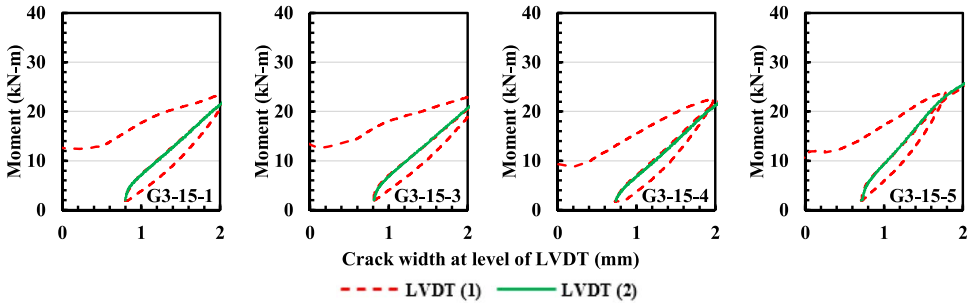

Fig. 17. Moment versus crack width for beams reinforced with No. 5 (SI equivalent: 15M) GFRP3 bars.

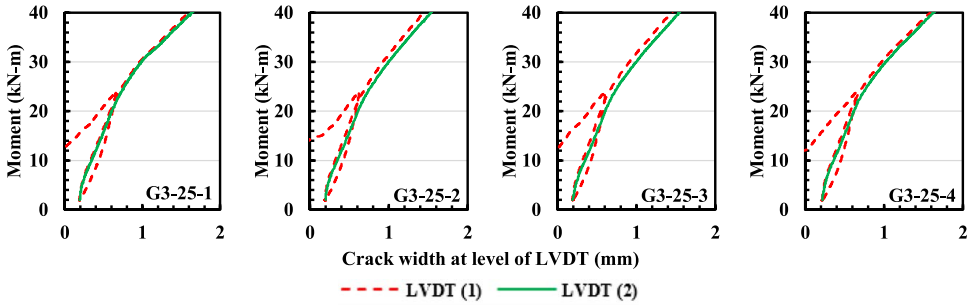

Fig. 18. Moment versus crack width for beams reinforced with No. 8 (SI equivalent: 25M) GFRP3 bars.

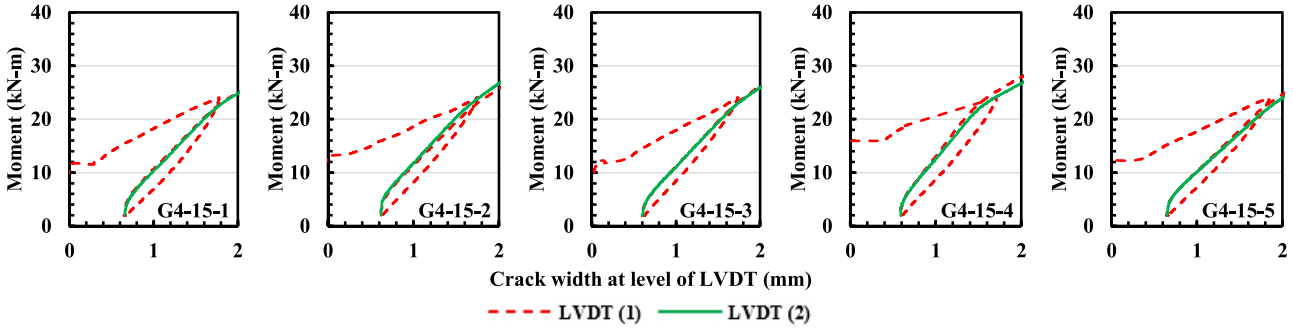

Fig. 19. Moment versus crack width for beams reinforced with No. 5 (SI equivalent: 15M) GFRP4 bars.

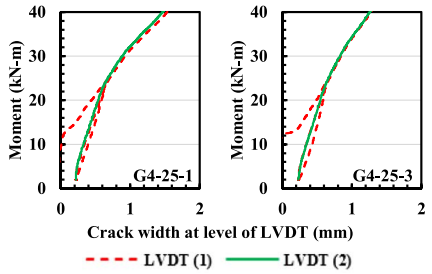

Fig. 20. Moment versus crack width for beams reinforced with No. 8 (SI equivalent: 25M) GFRP4 bars.

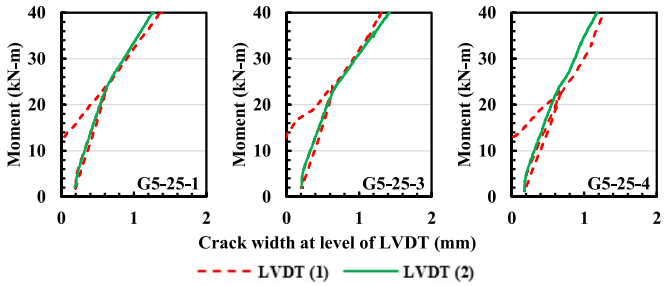

Fig. 22. Moment versus crack width for beams reinforced with No. 8 (SI equivalent: 25M) GFRP5 bars.

for the No. 5 bar specimens and 0.57 mm for the No. 8 bar specimens would correspond to 0.71 mm wide cracks at the tension face of the members.

The beams reinforced with No. 5 GFRP bars were loaded well above the 0.71 mm crack-width limit during the initial loading, whereas the beams reinforced with No. 8 GFRP bars were loaded to just about 0.71 mm, and the beams reinforced with steel bars were not loaded to this level of cracking. The crack widths at the first peak load are highly consistent for the beams reinforced with No. 8 GFRP bars with very little scatter for each type of GFRP bar. The crack widths for the beams with No. 5 GFRP bars varied significantly, especially by surface deformation type of the GFRP bars.

Process for Determining k_b as a Function of the First Crack Width. Values of k_b were determined using Eq. (1) at each load step for the crack widths measured by both LVDTs (1) and (2). Fig. 26 shows a plot of k_b versus the extrapolated crack width at the bottom of the beam ($w_{\text{bottom fiber}}$) for Beam G2-15-1 using LVDT (1) data starting immediately after cracking (through the rest of the first phase of loading), through the unloading phase, and then through the second phase of loading. The arrows on the figure show the parts of the curve associated with each loading phase (first phase of loading, unloading, and second phase of loading). Note that the reloading phase matches up with the initial loading phase when the crack width matches up. Therefore, had there not been unloading and reloading, the curve would have gone from A to B to D without the departure at B to C. The initial loading phase has k_b increasing with increasing crack widths, which is consistent with what Newhook (2000) found. The reloading phase has k_b decreasing with crack width until the crack width gets larger than the largest value obtained during the initial loading. This seems to imply that getting a k_b equivalent to that with the CSA S806-12 (CSA 2012) method, the unloading needs to occur prior to a crack width of 0.71 or 0.41 mm for the GFRP- or steel-RC beams, respectively. As shown in Fig. 26, unloading for this specimen occurred at a bottom fiber crack width of approximately 1.5 mm. Therefore, the proposed test method should be modified in future experiments when testing No. 5 GFRP or smaller bars by considering the appropriate geometric beam dimensions to limit the crack width prior to unloading to 0.71 mm or less for the GFRP–RC beams.

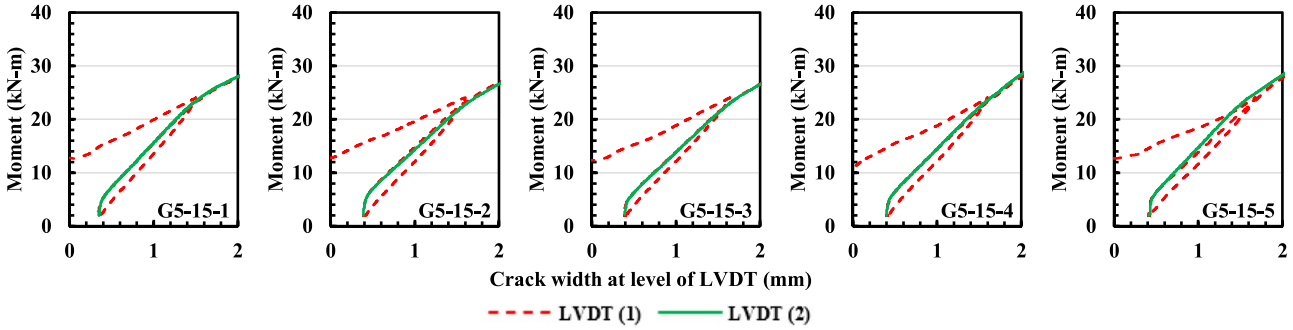

Fig. 21. Moment versus crack width for beams reinforced with No. 5 (SI equivalent: 15M) GFRP5 bars.

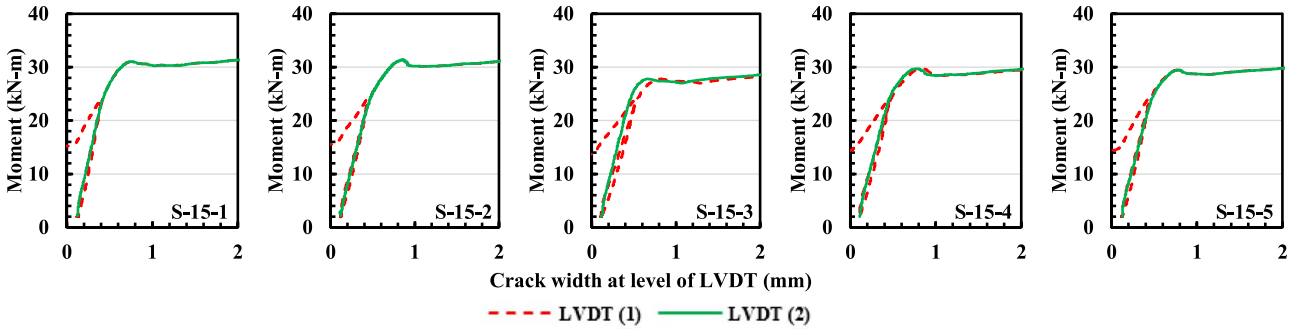

Fig. 23. Moment versus crack width for beams reinforced with 15M steel bars.

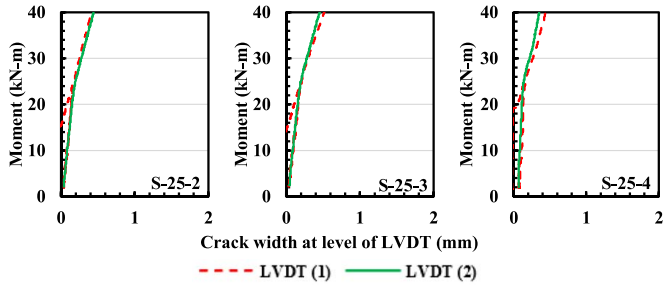

Fig. 24. Moment versus crack width for beams reinforced with 25M steel bars.

Similar to Fig. 26, Fig. 27 shows k_b versus the extrapolated crack width at the bottom of the beam ($w_{\text{bottom fiber}}$) but now using LVDT (2), which was present only during the reloading phase. The figure also includes a vertical line at 0.71 mm, which represents the crack width of interest. As can be seen, k_b can be determined with crack widths measured by both LVDTs with little difference for this beam. A further investigation of Fig. 27 shows two significantly different values of k_b for a crack width of 0.71 mm, depending on whether the initial loading or reloading is used. If the initial loading is used, k_b is 0.59; if the reloading is used, k_b is around 1.15–1.19, depending on which LVDT is used. If the loading had been stopped a bit later, the 0.71 mm line might have fallen on the steep part of the reloading curve (first part of C to B in Fig. 26), in which case small errors in adjusting the LVDTs could cause large changes in the k_b value.

The location of the unloading loop is quite different between the specimen with the No. 5 GFRP bars and the No. 8 GFRP bars. Fig. 28 shows the same plot for Beam G2-25-1 as Fig. 27 shows for Beam G2-15-1. For Beam G2-25-1, all of the unloading occurred prior to a crack width of 0.71 mm, and the k_b value of 0.95 originated from the backbone curve (the curve without unloading and reloading till the first peak load). Most of the No. 8 GFRP specimens had the unloading start very close to a crack width of 0.71 mm, and hence, the reloading was approximately 100% complete prior to achievement of a crack width of 0.71 mm, whereas the reloading was more typically about 50% complete for the beams with No. 5 GFRP bars; therefore, k_b values were determined from the first time an extrapolated bottom fiber crack width of 0.71 mm was reached.

Experimentally Determined k_b Values

Fig. 29 shows k_b values obtained using LVDT (1) data on the initial loading when the initial loading exceeded a crack opening of 0.71 or 0.41 mm for the GFRP- or steel-RC beams, respectively; when the initial loading did not reach the desired crack width, k_b was obtained from data during the second loading phase.

Table 4 summarizes the k_b values for each beam tested. For the No. 8 GFRP bars, the average k_b values were 0.97, 0.97, 0.97, 0.99, and 0.98 for GFRP1, GFRP2, GFRP3, GFRP4, and GFRP5 bars, respectively. On the other hand, the average k_b values for the same types of No. 5 GFRP bars were 0.55, 0.58, 0.71, 0.64, and 0.59, respectively. For the No. 8 bars, there was no significant difference in k_b values between the different bar types. For the No. 5 bars, GFRP1, GFRP2, and GFRP5 all had very similar k_b values. Some of these bars were sand-coated and some were not. The distinction in ACI 440.1R-15 (ACI 2015) for different k_b values between sand-coated bars and bars without a sand coating is not supported by the current results. The results also show a clear correlation between bar size and k_b, with larger bars having a larger value of k_b. Therefore, the new data on the new generation of GFRP bars would suggest a k_b value of 1.00 for No. 8 bars and smaller. On the other hand, the old database of the early generation of GFRP bars contains enough data showing a k_b greater than 1.00.

Table 3. Error estimates between LVDT (1) and LVDT (2)

Beam	Bar size	MAPE (%)
G1-15-1[a]	No. 5	—
G1-15-2[a]	No. 5	—
G1-15-3[a]	No. 5	—
G1-15-4	No. 5	1.18
G1-15-5	No. 5	0.24
G2-15-1	No. 5	0.90
G2-15-2	No. 5	2.49
G2-15-3	No. 5	1.66
G2-15-4	No. 5	2.17
G2-15-5	No. 5	1.12
G3-15-1	No. 5	—
G3-15-2[a]	No. 5	—
G3-15-3	No. 5	—
G3-15-4	No. 5	—
G3-15-5	No. 5	—
G4-15-1	No. 5	—
G4-15-2	No. 5	—
G4-15-3	No. 5	—
G4-15-4	No. 5	—
G4-15-5	No. 5	—
G5-15-1	No. 5	1.73
G5-15-2	No. 5	0.57
G5-15-3	No. 5	0.87
G5-15-4	No. 5	1.24
G5-15-5	No. 5	1.62
S-15-1	15M	2.28
S-15-2	15M	1.97
S-15-3	15M	8.26
S-15-4	15M	9.85
S-15-5	15M	2.04
G1-25-1	No. 8	0.21
G1-25-2[b]	No. 8	—
G1-25-3	No. 8	0.11
G1-25-4	No. 8	0.18
G1-25-5	No. 8	0.10
G2-25-1	No. 8	2.12
G2-25-2	No. 8	3.65
G2-25-3	No. 8	3.49
G2-25-4	No. 8	1.31
G2-25-5	No. 8	0.80
G3-25-1	No. 8	2.58
G3-25-2	No. 8	3.30
G3-25-3	No. 8	4.14
G3-25-4	No. 8	3.25
G3-25-5[b]	No. 8	—
G4-25-1	No. 8	2.80
G4-25-2[b]	No. 8	—
G4-25-3	No. 8	1.24
G4-25-4[a]	No. 8	—
G4-25-5[a]	No. 8	—
G5-25-1	No. 8	2.78
G5-25-2[b]	No. 8	16.61
G5-25-3	No. 8	1.81
G5-25-4	No. 8	5.21
G5-25-5[b]	No. 8	3.03
S-25-1[a]	25M	—
S-25-2	25M	10.21
S-25-3	25M	17.14
S-25-4	25M	8.85
S-25-5[b]	25M	—

Note: MAPE = mean absolute percentage error.
[a]The first crack was not where there is only one bar.
[b]No data from LVDT (1).

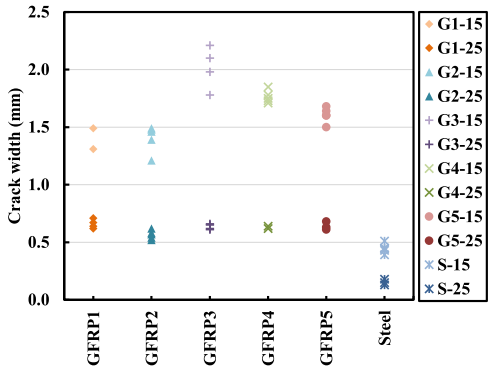

Fig. 25. Crack width at the height of the bar measured by LVDT (1) at the first peak load.

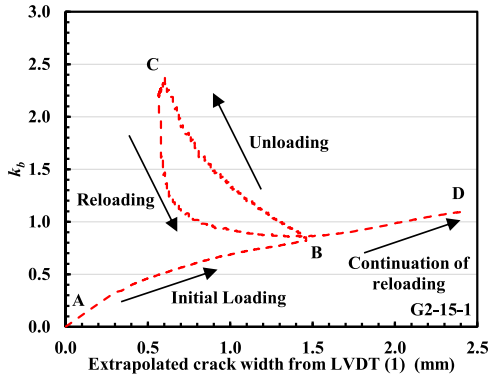

Fig. 26. k_b versus extrapolated crack width from LVDT (1).

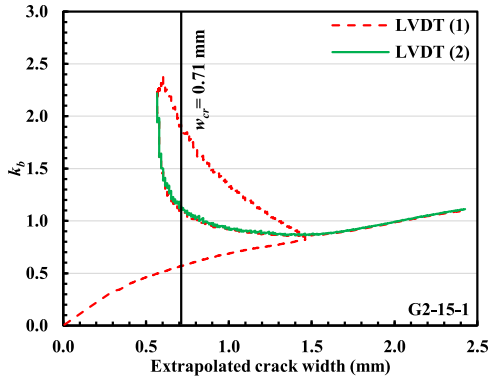

Fig. 27. k_b versus extrapolated crack width from each LVDT for Beam G2-15-1.

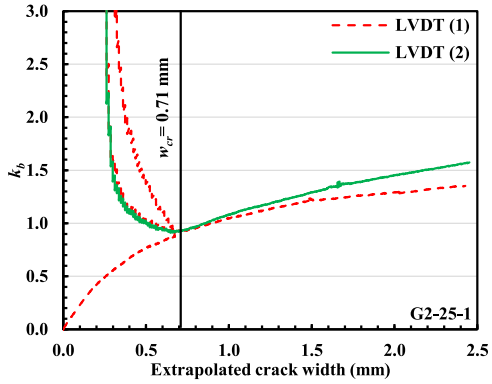

Fig. 28. k_b versus extrapolated crack width from each LVDT for Beam G2-25-1.

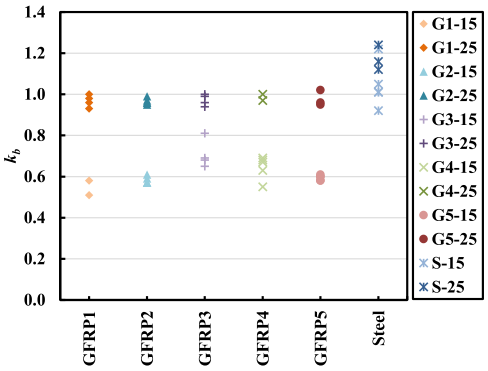

Fig. 29. k_b based on LVDT (1) during initial loading.

Therefore, to be conservative, the authors recommend the use of the bond-dependent coefficient k_b of 1.20 from ACI CODE 440.11-22 (ACI 2022): *Structural Concrete Buildings Reinforced Internally with Fiber-Reinforced Polymer (FRP) Bars*.

Table 4. k_b values for No. 5 and No. 8 bars

Beam ID	k_b	Bar size	Average k_b	SD	COV (%)
G1-15-1[a]	—	No. 5	0.55	0.05	9.1
G1-15-2[a]	—				
G1-15-3[a]	—				
G1-15-4	0.51				
G1-15-5	0.58				
G2-15-1	0.59	No. 5	0.58	0.02	3.1
G2-15-2	0.57				
G2-15-3	0.57				
G2-15-4	0.61				
G2-15-5	0.57				
G3-15-1	0.68	No. 5	0.71	0.07	10.0
G3-15-2[a]	—				
G3-15-3	0.65				
G3-15-4	0.81				
G3-15-5	0.69				
G4-15-1	0.67	No. 5	0.64	0.06	8.9
G4-15-2	0.63				
G4-15-3	0.69				
G4-15-4	0.55				
G4-15-5	0.68				
G5-15-1	0.58	No. 5	0.59	0.02	2.6
G5-15-2	0.58				
G5-15-3	0.61				
G5-15-4	0.60				
G5-15-5	0.60				
S-15-1	0.92	15M	1.04	0.11	10.5
S-15-2	1.01				
S-15-3	1.22				
S-15-4	1.05				
S-15-5	1.01				
G1-25-1	1.00	No. 8	0.97	0.03	3.1
G1-25-2[b]	—				
G1-25-3	0.96				
G1-25-4	0.98				
G1-25-5	0.93				
G2-25-1	0.96	No. 8	0.97	0.02	1.6
G2-25-2	0.96				
G2-25-3	0.99				
G2-25-4	0.95				
G2-25-5	0.97				
G3-25-1	0.99	No. 8	0.97	0.03	2.8
G3-25-2	0.96				

Table 4. (*Continued*.)

Beam ID	k_b	Bar size	Average k_b	SD	COV (%)
G3-25-3	0.94				
G3-25-4	1.00				
G3-25-5[b]	—				
G4-25-1	0.97	No. 8	0.99	0.02	2.2
G4-25-2[b]	—				
G4-25-3	1.00				
G4-25-4[a]	—				
G4-25-5[a]	—				
G5-25-1	0.95	No. 8	0.98	0.04	3.9
G5-25-2[b]	—				
G5-25-3	0.96				
G5-25-4	1.02				
G5-25-5[b]	—				
S-25-1[a]	—	25M	1.17	0.06	5.2
S-25-2	1.12				
S-25-3	1.24				
S-25-4	1.16				
S-25-5[b]	—				

Note: The SI equivalents for No. 5 and No. 8 bars are 15M and 25M, respectively.
[a]The first crack was not where there is only one bar.
[b]No data from LVDT (1).

Conclusions

For design purposes, the bond-dependent coefficient k_b should be used to check the crack width in flexural concrete members reinforced with GFRP bars at service load. This coefficient accounts for the degree of bond between the GFRP bars and the surrounding concrete. Sixty RC beams were tested to assess the bond-dependent coefficient for five types of commercially available GFRP bars: GFRP1, with a deformed/ribbed surface; GFRP2, with a helically deformed surface; GFRP3, with a helically grooved surface; GFRP4, with a double-helical wrap/sand-coated surface; and GFRP5, with a sand-coated surface. Two bar sizes (No. 5 and No. 8)—representing bars used in practice as longitudinal reinforcement in flexural concrete members—were tested for each of the bar types. The GFRP bars that were tested are currently available on the market and have a modulus of elasticity of approximately 60 GPa. Based on the experimental results and their analysis, the main findings of this investigation are as follows:

1. Experimentally determined k_b values for No. 5 and No. 8 new-generation GFRP bars were found to be no larger than 1.00 for the concrete strength, cover, and spacing used in these tests.
2. There is no observable difference between the k_b values for bars that are sand-coated and bars with different surface deformations for the same bar size. Therefore, a distinction between types of surface-deformation bars is not required, and, a k_b value of 1.20 is recommended for all bar types that satisfy ASTM D7957/D7957M-22 (ASTM 2022).
3. The assumed relationship between crack width and bar stress (applied moment) does not accurately reflect the physics of the phenomenon. According to the current formula, k_b should not be a function of bar size, yet the data collected clearly indicate different values of k_b for No. 5 and No. 8 bars.
4. The reproducibility of the test results was surprisingly good, given that concrete cracking was intended to occur. However, the proposed test method requires some modification to ensure that the width of the first crack at the bottom face of the beam is less than 0.71 mm during the initial loading phase. The crack width immediately after cracking for the beams reinforced with No. 5 bars was larger than 0.71 mm; thus, it is recommended that the beam dimensions be adjusted when testing beams with smaller bars to limit the crack width after cracking (before unloading) to be less than 0.71 mm.
5. Future experimental and analytical investigations should be conducted to examine the effect of concrete strength, concrete cover, and bar spacing on the k_b value.
6. The k_b value is dependent on the size of the crack width that is used in the evaluation, so a comparison of k_b from different research works that use different-size crack widths is problematic. Evaluation of k_b should be based on the same size crack width for ease of comparison; the authors recommend the use of a 0.71 mm crack width at the extreme tension face of beam specimens in the evaluation of k_b for GFRP bars.

Appendix. Example Calculation of Bond-Dependent Coefficient (k_b)

A simply supported beam, G2-25-1, with a cross-sectional width and height of 200 and 360 mm, respectively, was tested up to failure. The beam was reinforced with one No. 8 GFRP2 bar as longitudinal reinforcement. The GFRP2 bar had a helically deformed surface with a nominal diameter of 25.4 mm and $E_f = 63{,}000$ MPa. The clear concrete cover to the stirrups was 38 mm.

Determine the bond-dependent coefficient at the crack width of 0.71 mm using Eq. (1).

Given:

$b = 200$ mm, $h = 360$ mm, Bottom clear cover to stirrups = 38 mm. $d_{\text{stirrup}} = 9.5$ mm.

$f'_c = 41.7$ MPa.

No. of bars = 1 bar. $E_f = 63{,}000$ MPa. $d_b = 25.4$ mm. $A_f = 510$ mm^2.

Solution:

$$d = h - \text{clear cover} - d_{\text{stirrup}} - \left(\frac{d_b}{2}\right) = 360 - 38 - 9.5 - \left(\frac{25.4}{2}\right) = 299.80 \text{ mm}$$

$$d_c = \text{clear cover} + d_{\text{stirrup}} + \left(\frac{d_b}{2}\right) = 38 + 9.5 + \left(\frac{25.4}{2}\right) = 60.20 \text{ mm}$$

$$E_c = 4{,}700\sqrt{f'_c} = 4{,}700\sqrt{41.7} = 30{,}350 \text{ MPa}$$

$$n_f = \frac{E_f}{E_c} = \frac{63{,}000}{30{,}350} = 2.08$$

$$\rho_f = \frac{A_f}{bd} = \frac{1 \times 510}{200 \times 299.80} = 0.0085$$

$$k = \sqrt{2\rho_f n_f + (\rho_f n_f)^2} - \rho_f n_f$$

$$k = \sqrt{(2 \times 0.0085 \times 2.08) + (0.0085 \times 2.08)^2} - (0.0085 \times 2.08) = 0.1711$$

$$c = kd = 0.1711 \times 299.80 = 51.29 \text{ mm}$$

$$\beta = \frac{h - c}{d - c} = \frac{360 - 51.34}{299.30 - 51.34} = 1.24$$

J. Compos. Constr., 2023, 27(6): 04023057

$$I_{cr} = \frac{bd^3}{3}k^3 + n_f A_f d^2 (1-k)^2$$

$$I_{cr} = \left(\frac{200 \times 299.80^3}{3} \times 0.1711^3\right) + (2.08 \times 510 \times 299.80^2 \times (1-0.1711)^2)$$

$$I_{cr} = 74{,}373{,}260\,\text{mm}^4$$

$$w_{\text{side face}} = \frac{w_{cr}}{\beta} = \frac{0.71}{1.24} = 0.57\,\text{mm}$$

$$\text{At } w_{\text{side face}} = 0.57\,\text{mm}: M = 23.10\,\text{kN}-\text{m}$$

$$f_f = n_f \times \frac{My}{I_{cr}}$$

$$f_f = 2.08 \times \frac{23.10 \times 1{,}000{,}000 \times (299.80 - 51.29)}{74{,}373{,}260} = 160.25\,\text{MPa}$$

$$k_b = \frac{w_{cr}}{2 \times \frac{f_f}{E_f} \times \beta \times \sqrt{d_c^2 + (s/2)^2}}$$

$$k_b = \frac{0.71}{2 \times \frac{160.25}{63{,}000} \times 1.24 \times \sqrt{60.20^2 + 100^2}} = 0.96$$

Data Availability Statement

All data, models, and code generated or used during the study appear in the published article.

Acknowledgments

The research presented herein was funded by the Natural Sciences and Engineering Research Council of Canada (NSERC. The donation of GFRP bars by Owens Corning (Concord, NC, USA), Pultrall Inc. (Thetford Mines, QC, Canada), B&B FRP Manufacturing Inc. (Toronto, ON, Canada), TUFBAR Canada Inc. (Edmonton, AB, Canada), and ASA.TEC GMBH (Langenlois, Austria) to support this investigation are greatly appreciated. The authors would like to express their special thanks to Jerome Lacroix, Pascal St-Laurent, and Steven MacEachern, technicians in the Department of Civil Engineering at the University of Sherbrooke, for their help during casting and testing of the reinforced concrete beams.

Notation

The following symbols are used in this paper:

A_f = area of tension GFRP bar (mm^2);
A_{im} = immersed cross-sectional area (mm^2);
b = beam width (mm);
c = distance from the extreme compression fiber to the elastic cracked section neutral axis (mm);
c_c = clear concrete cover (mm);
d = distance from the compression face of the concrete to the center of the tension FRP bars (mm);
d_b = bar diameter (mm);
d_c = distance from the center of the tension bar to the tension face of the concrete (mm);
d_{stirrup} = stirrup diameter (mm);
E_c = modulus of elasticity of the concrete (MPa);
E_f = modulus of elasticity of the GFRP reinforcement (MPa);
E_s = modulus of elasticity of the steel bars (MPa);
f'_c = specified compressive strength of the concrete (MPa);
f_{fu} = ultimate strength of the tension GFRP bars (MPa);
f_f = GFRP bar stress (MPa);
f_y = yield strength of the steel bars (MPa);
h = beam height (mm);
I_{cr} = moment of inertia of the cracked transformed section (mm^4);
k = ratio of the neutral-axis depth to the reinforcement depth;
k_b = bond-dependent coefficient;
M = applied moment (kN·m);
M_{cr} = theoretical cracking moment (kN·m);
n_f = modular ratio;
s = bar spacing (mm);
w_{cr} = crack width on the tension face (mm);
$w_{\text{side face}}$ = crack width at the level of the reinforcement (mm);
y = distance from the centroid of the cracked transformed section to the centroid of the reinforcing bar;
β = amplification factor that accounts for the strain gradient;
ε_{fu} = ultimate strain of the GFRP bars;
ε_y = yield strain of steel bars; and
ρ_f = longitudinal reinforcement ratio of the tension GFRP bars.

References

ACI (American Concrete Institute). 2015. *Guide for the design and construction of concrete reinforced with FRP bars*. ACI 440.1R-15. Farmington Hills, MI: ACI.

ACI (American Concrete Institute). 2019. *Building code requirements for structural concrete and commentary*. ACI 318R-19. Farmington Hills, MI: ACI.

ACI (American Concrete Institute). 2022. *Building code requirements for structural concrete reinforced with glass fiber-reinforced polymer (GFRP) bars—Code and commentary*. ACI 440.11-22. Farmington Hills, MI: ACI.

ASTM. 2021. *Standard test method for compressive strength of cylindrical concrete specimens*. ASTM C39/C39M-21. West Conshohocken, PA: ASTM.

ASTM. 2022. *Standard specification for solid round glass fiber reinforced polymer bars for concrete reinforcement*. ASTM D7957/D7957M-22. West Conshohocken, PA: ASTM.

Benmokrane, B., S. Mehany, C. Shield, A. Nanni, and V. Brown. 2023. "Physical properties, longitudinal tensile properties, and bond strength of the new generation of GFRP bars." *J. Compos. Constr.* 27 (6). https://doi.org/10.1061/JCCOF2.CCENG-4300.

Benzecry, V., A. R. Emparanza, F. D. C. Basalo, and A. Nanni. 2021. "Bond coefficient, k_b, of GFRP bars." *Constr. Build. Mater.* 292: 123380. https://doi.org/10.1016/j.conbuildmat.2021.123380.

CSA (Canadian Standards Association). 2012. *Re-approved in 2021—"Design and construction of building components with fiber reinforced polymers"*. CSA S806-12. Rexdale, ON, Canada: CSA.

CSA (Canadian Standards Association). 2019. *Specification for fibre-reinforced polymers*. CSA S807-19. Rexdale, ON, Canada: CSA

Elgabbas, F., E. A. Ahmed, and B. Benmokrane. 2017. "Flexural behavior of concrete beams reinforced with ribbed basalt-FRP bars under static loads." *J. Compos. Constr.* 21 (3): 04016098. https://doi.org/10.1061/(ASCE)CC.1943-5614.0000752.

El-Nemr, A., E. Ahmed, C. Barris, and B. Benmokrane. 2016. "Bond dependent coefficient of glass and carbon FRP bars in normal and high

strength concretes." *J. Constr. Build. Mater.* 113 (1): 77–89. https://doi.org/10.1016/j.conbuildmat.2016.03.005.
El-Salakawy, E. F., and B. Benmokrane. 2004. "Serviceability of concrete bridge deck slabs reinforced with FRP composite bars." *ACI Struct. J.* 101 (5): 727–736.
Frosch, R. J. 1999. "Another look at cracking and crack control in reinforced concrete." *ACI Struct. J.* 96 (3): 437–442.
Mehany, S., H. M. Mohamed, A. El-Safty, and B. Benmokrane. 2021a. "Bond-dependent coefficient and cracking behavior of lightweight self-consolidating concrete (LWSCC) beams reinforced with glass- and basalt-FRP bars." *Constr. Build. Mater.* 329: 127130. https://doi.org/10.1016/j.conbuildmat.2022.127130.
Mehany, S., H. M. Mohamed, and B. Benmokrane. 2021b. "Flexural strength and serviceability of GFRP-reinforced lightweight self-consolidating concrete beams." *J. Compos. Constr.* 26 (3): 04022020. https://doi.org/10.1061/(ASCE)CC.1943-5614.0001208.
Newhook, J. P. 2000. "The use of fibre reinforced concrete to reduce crack widths in GFRP reinforced concrete beams." In *Proc., 3rd Int. Conf. Advanced Composite Materials in Bridges and Structures*, 145–152. Montreal, QC: Canadian Society of Civil Engineering.
Shield, C., V. Brown, C. E. Bakis, and S. Gross. 2019. "A recalibration of the crack width bond-dependent coefficient for GFRP-reinforced concrete." *J. Compos. Constr.* 23 (4): 04019020. https://doi.org/10.1061/(ASCE)CC.1943-5614.0000978.